

Isotropic conduction and negative photoconduction in ultrathin PtSe₂ films

Francesca Urban^{1,2,3}, Farzan Gity⁴, Paul K. Hurley⁴, Niall McEvoy⁵, and Antonio Di Bartolomeo^{1,2,*}

¹ Physics Department, University of Salerno, via Giovanni Paolo II, 132, 84084 Fisciano, Salerno, Italy

² CNR-Spin, via Giovanni Paolo II, 132, 84084 Fisciano, Salerno, Italy

³ INFN-Gruppo collegato di Salerno, via Giovanni Paolo II, 132, 84084 Fisciano, Salerno, Italy

⁴ Tyndall National Institute, University College Cork, Cork, Ireland

⁵ AMBER & School of Chemistry, Trinity College Dublin, Dublin 2, Ireland

* Correspondence: adibartolomeo@unisa.it

Received: date; Accepted: date; Published: date

Abstract: PtSe₂ ultrathin films are used as the channel of back-gated field-effect transistors (FETs) that are investigated at different temperatures and under super-continuous white laser irradiation. The temperature-dependent behavior confirms the semiconducting nature of multilayer PtSe₂, with p-type conduction, a hole field-effect mobility up to $40 \text{ cm}^2 \text{V}^{-1} \text{s}^{-1}$ and significant gate modulation. Electrical conduction measured along different directions shows isotropic transport. A reduction of PtSe₂ channel conductance is observed under exposure to light. Such a negative photoconductivity is explained by a photogating effect caused by photo-charge accumulation in SiO₂ and at the Si/SiO₂ interface.

Keywords: PtSe₂; field effect transistor; laser irradiation; electrical conduction; temperature; negative photoconductivity;

The family of transition-metal dichalcogenides (TMDs), such as the most known MoS₂, WSe₂, WS₂, has been heavily investigated over the last decade due to their intriguing and layer-tunable properties combined with their ease of fabrication ¹⁻⁷. The bulk materials, made of atomic layers held together by van der Waals forces, can be easily exfoliated to obtain single- or few-layer nanosheets ^{8,9} and the electrical and optical properties of these materials are strongly dependent on their thickness ^{10,11}. Indeed, the modulation of bandgap via changing the number of layers enables the use of TMDs as field-effect transistor (FET) channels in optical sensors with high photo-response ^{12,13}. Moreover, the intrinsic n- or p-type doping is useful for the construction of p-n heterojunctions ¹⁴⁻¹⁶.

To date, in addition to the exfoliation methods, various scalable and controllable growth techniques, mostly based on chemical vapor deposition (CVD) and laser ablation, have been developed, enabling the synthesis of large-area flakes with fine thickness control and consequent tailoring of the chemical, optical and electrical properties ¹⁷⁻¹⁹.

Different from MoS₂, WSe₂ or other group-6 TMDs, dichalcogenides based on group-10 transition metals have just recently gained popularity and not been fully explored yet.

Platinum diselenide (PtSe₂) and ditelluride (PtTe₂), along with their palladium analogues, were theoretically predicted in the sixties of the last century but have only recently been isolated and investigated as 2D materials^{20–26}. Numerical calculations of their electronic structure and properties encouraged their use in electronic applications. These materials crystallize in an octahedral lattice structure where the transition metal atoms are coordinated with six chalcogens. Each layer is a two-dimensional packed array of metal atoms sandwiched between two similar arrays of chalcogens, and bonded by van der Waals forces to form the multilayer structure. The main difference between TMDs of group 6 and the group 10 is that the presence of d-electrons in the group-10 transition metals gives rise to additional semiconductor bands²⁰.

PtSe₂, the material under study in this paper, is a semimetal in bulk form, with slightly indirect overlap of the conduction and valence bands, that undergoes a semimetal-to-semiconductor transition when it is thinned to a few atomic layers^{27–29}. Monolayer PtSe₂ has an indirect bandgap of ~1.2 eV, which is expected to reduce to 0.3 eV for the bilayer^{22,30}. The variability of electrical properties, combined with environmental stability, is attracting growing attention from both fundamental and application standpoints. For instance, the bandgap covers the spectral range that is important for telecommunications and solar energy harvesting³¹, and the carrier mobility (theoretically predicted up to 4000 cm²V⁻¹s⁻¹³² and experimentally found to be around 200 cm²V⁻¹s⁻¹^{33,34}), competitive with black phosphorus, can enable fast electronic devices^{33,35–37}. Other interesting properties include the catalytic activity^{38,39} and the sensitivity to analytes such as NO₂, NO, NH₃ or ethanol^{40,41}. Furthermore, the direct selenization of platinum films on a chosen substrate, and the rather low temperatures (400 °C) required for the thermally assisted synthesis of PtSe₂, might give this material a boost for integration in semiconductor technologies for mass production^{21,22,28}.

In this work, we study the electrical conduction in multilayer PtSe₂ sheets along orthogonal directions using back-gated field-effect transistors. The electrical behavior is analyzed over a wide temperature range demonstrating semiconducting p-type conduction, with reasonable gate modulation and relatively high hole mobility. The electrical conduction along orthogonal directions does not show any significant difference and the intrinsic p-type behavior of the transistors is stable under air exposure. Laser irradiation reveals more complex phenomena than the usual current increase by photo-generation. Indeed, excitation by laser pulses unexpectedly reduces the channel conductance. We explain such a negative photoconductivity (NPC) as occurring due to a photogating effect, which arises from photocharge accumulation in the SiO₂ dielectric and at the Si/SiO₂ interface.

The devices were fabricated over Si/SiO₂ substrate (85 nm thermally grown oxide on p-type silicon, $\rho \sim 0.001 - 0.005 \Omega cm$). The PtSe₂ film on SiO₂ was obtained by direct selenization of a previously sputtered Pt film (nominal thickness 0.7 nm) following procedures described elsewhere⁴⁰. Briefly, Pt films were placed in the center of the downstream zone of a two-zone furnace where they were heated to 400 °C. Se pellets were independently heated to 220 °C in the upstream zone and 150 sccm of Ar:H₂ (90%:10%) carried Se vapor from

the upstream to the downstream zone, where it reacted with the Pt films. A growth time of 2 hours ensured that Pt was completely converted to PtSe₂. During this process the film thickness increases by a factor of $\sim 3.5 - 4$ ²¹.

The PtSe₂ film was transferred using a polymer-based process from the growth substrate to a fresh Si/SiO₂ substrate²⁹, and it was then patterned using photoresist masking and a SF₆-based inductively coupled plasma (ICP) etching process. This was followed by patterning Ni: Au (20 nm : 150 nm) metal contacts using a standard lift-off process.

The as-synthesized PtSe₂ film has a 1T crystal structure, where six selenium atoms are bonded to a platinum atom located at the center of an octahedral geometry, as shown in Figure 1(a)⁴². The lattice in a top view (see Figure 1(b)) appears as two hexagonal arrays, shifted with respect to each other, with Pt (yellow spheres) and Se (blue spheres) atoms centering the basis^{40,43}.

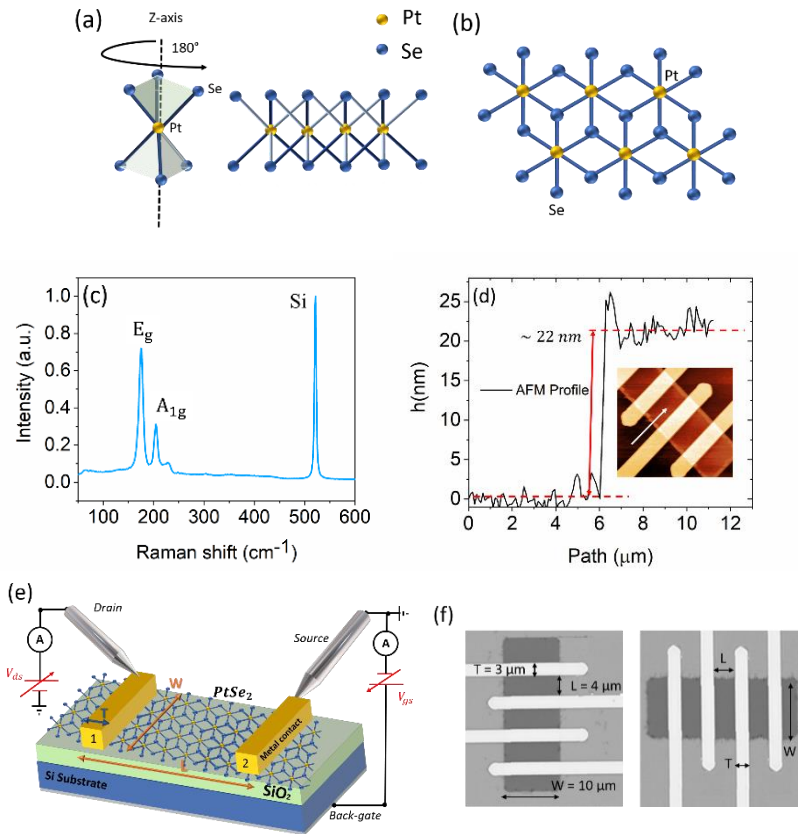


Figure 1. (a) Scheme of the octahedral basis and layered structure of PtSe₂ layer and (b) its hexagonal top viewed array. (c) Raman characterization of the prepared PtSe₂ sheet, showing the two PtSe₂ peaks at 176 cm^{-1} and 205 cm^{-1} , and the Si peak. (d) AFM image and step height profile. (e) Schematic of the measurement setup. (f) Optical images of two selected devices in the horizontal and vertical configuration.

Raman spectroscopy was used to characterize the as-synthesized films. The characteristic E_g ($\sim 176 \text{ cm}^{-1}$) and A_{1g} ($\sim 205 \text{ cm}^{-1}$) modes (see Figure 1(c)) were observed confirming the successful synthesis of PtSe₂. The position and relative intensity of these modes is consistent with the synthesis of multilayer PtSe₂⁴³. The step height measured by AFM (Figure 1(d)) is $\sim 22 \text{ nm}$ and includes the 19 nm SiO₂

over-etch applied during the PtSe₂ film patterning. Therefore, the thickness of PtSe₂ is ~ 3 nm, corresponding to about 6 layers (PtSe₂ monolayer is 0.5 nm thick⁴⁴).

The devices were measured in two- and four-probe configurations in a Janis Probe Station (Janis ST-500 probe station) equipped with four nanoprobe connected to a Keithley 4200 SCS (semiconductor characterization system), under different conditions. A scheme of the contacted back-gated device is shown in Figure 1(e): The metal contacts were used as the drain and source electrodes while the probe station chuck, connected to the silicon substrate, provided the gate voltage.

The following analysis was conducted on two main types of devices, having the same channel length (L) and width (W) and contact leads (T) in the direction of the channel. The devices were fabricated from the same PtSe₂ sheet, simultaneously patterned to form a horizontal and a vertical channel, an example is displayed by the optical microscope images of Figure 1(f). Identical contacts, differing only in orientation, allow the measurement of the channel conductance in the two perpendicular directions.

The electrical measurements were performed at a constant air pressure of 10^{-3} mbar and at different temperatures, as well as in dark conditions and under irradiation from a super-continuous laser source (NKT Photonics, Super Compact, wavelength ranging from 450 nm to 2400 nm, at 30 mW/cm²).

Using the two-probe configuration, we studied the variation of the PtSe₂ conductance G as a function of temperature T from 400 K to near liquid-nitrogen temperature. The G - T curves for the horizontal and vertical samples, reported in Figure 2(a), show similar trends with the channel conductance decreasing when T is slowly cooled down from 400 K to 90 K. The G - T behavior reveals the semiconducting nature of PtSe₂ ultrathin films.

The I-V current-voltage characteristics, at zero gate voltage, in two- and four-probe configurations, are reported in the inset of Figure 2(a), for both the two chosen horizontal- and the vertical-channel devices. The comparison of two- and four-probe measurements, with no appreciable difference, confirms the negligible effect of the metal contacts on the channel conductance as well as the ohmic behavior of the semiconductor/metal junctions, enabling the use of the two-probe configuration for further analysis.

To better understand the semiconducting nature of the material, we performed transfer characteristic measurements at two extreme temperatures, 290 K and 90 K. The gate voltage was intentionally limited between -10 and 10 V to avoid the breakdown of the 85 nm gate oxide. Figure 2(b) shows decreasing conductance for positive gate voltage, indicative of p-type intrinsic channel doping, and a modulation of a factor 2 in the narrow explored gate voltage range, consistent with the narrow bandgap of multilayer PtSe₂.

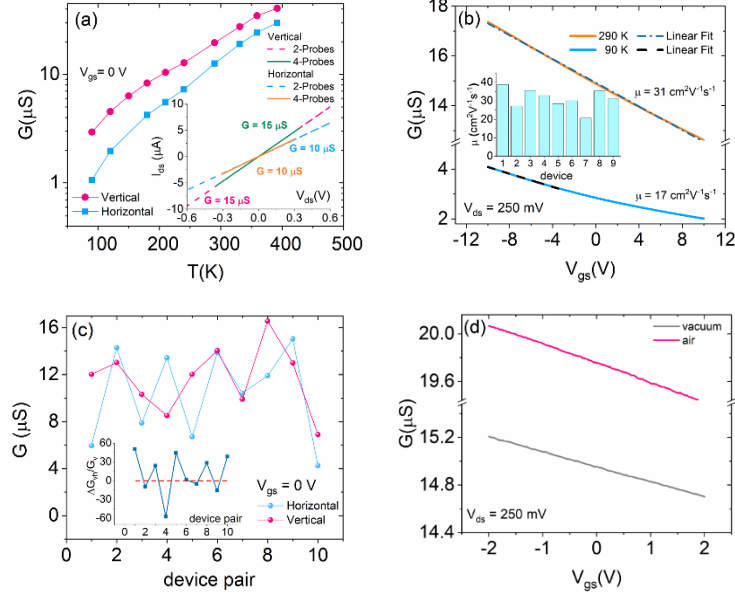


Figure 2. (a) G vs T curves for horizontal (cyan) and vertical (magenta) devices on semilogarithmic scale, at $V_{gs} = 0$ V; the inset shows the I - V characteristics for horizontal and vertical device in 2- (4-) probe configuration plotted in cyan dashed (orange straight) line and in magenta dashed (green straight) line, respectively. (b) Transfer characteristics at 90 K (cyan curve) and 290 K (orange) for the vertical device with the linear fits (black and blue dashed curves respectively) used to estimate the maximum hole mobility. The inset reports the hole mobility for different devices in an analog configuration. (c) Room temperature conductance for horizontal (cyan) and vertical (magenta) device pairs. Each pair is formed by a horizontal and a vertical device fabricated next to one another to avoid potential impact of thickness. The inset shows the percentile variation $\frac{\Delta G_{vh}}{G_v} = \frac{G_v - G_h}{G_v}$ between the two conductances for each device pair. (d) Transfer characteristics in vacuum $\sim 10^{-3}$ mbar (grey curve) and air (magenta curve), for the vertical device.

From the transfer characteristics, we evaluated the field effect mobility as $\mu = \frac{L}{WC_{ox}V_{ds}} \frac{dI_{ds}}{dV_{gs}}$ (V_{ds} is the source-drain bias and $C_{ox} = 3.11 \text{ nFcm}^{-2}$ is the SiO_2 capacitance per area), finding values in the range $15 - 40 \text{ cm}^2\text{V}^{-1}\text{s}^{-1}$ at room temperature (as reported in the inset of Figure 2(b) for the vertical devices) and $10 - 20 \text{ cm}^2\text{V}^{-1}\text{s}^{-1}$ at 90 K. The temperature dependence of the mobility is ascribed to Coulomb scattering due to fixed charges^{6,45}.

These values can be considered rather high if compared to the mobilities commonly reported for similar PtSe_2 or other TMD-based devices^{5,24,34,46-48}.

The electrical conductance of several pairs of horizontal and vertical devices, at room temperature and grounded gate, has been investigated and it is reported in Figure 2(c). The device pairs were chosen as close as possible to each other (few μm) to avoid potential impact of thickness between distant zones of the wafer. The plot shows that the conductance of horizontal and vertical devices have fluctuations up to 60% but originate distributions that are consistent with each other. Otherwise stated, Figure 2(c) demonstrates that conduction of PtSe_2 films is isotropic. The isotropic conduction is consistent with the observation of randomly-oriented grains in ultrathin PtSe_2 films reported elsewhere^{40,43,49}.

Finally, Figure 2(d) shows that passing from vacuum (~ 1 mbar) to ambient pressure does not change the channel doping from p-type to n-type as observed with other TMD materials, strongly influenced by the environmental atmosphere^{6,24,50,51}. The p-type behavior of PtSe₂ is preserved when changing either the chamber temperature or pressure, and the conduction enhancement in air is attributed to the p-doping of oxygen molecules, which are electron acceptors.

To further investigate the behavior of PtSe₂, we measured the electrical conduction of the device under pulsed laser irradiation, both in vacuum (10^{-3} mbar) and at room pressure.

Figure 3(a-b) show the device channel current under super-continuous laser irradiation, with the light switched on and off every two minutes for 12 cycles. The experiment was conducted with the laser source at 30 mW/cm^2 . After the on/off cycles, the laser is turned off and the device slowly returns to the initial conduction state. Surprisingly, each laser irradiation (on-pulse) induces a reduction of the current. This behavior, that is referred to negative photoconductivity, is opposite to the current increase normally observed under light as an effect of photo-generation^{52–55}.

It is important to note that the laser beam induces reversible changes in the irradiated device. The current lowering lasts for different periods of time, ranging from minutes to several hours. The comparison of Figure 3(a) and 3(b) shows that the restoration of the initial state is significantly faster in air at room pressure.

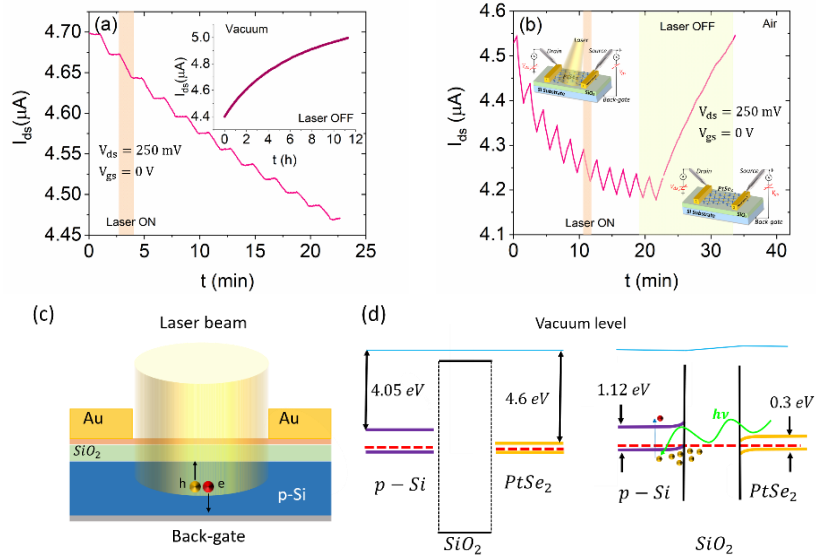


Figure 3. I_{ds} vs time characteristics under super-continuous laser beam irradiation, wavelength ranging from 450 nm to 2400 nm, at 10^{-3} mbar (a) and room pressure (b). The inset of panel (a) shows the recovery of the device current after several hours from the laser irradiation. (c) Schematic of the device under laser irradiation and (d) band diagram of the p-Si/SiO₂/PtSe₂ structure and charge accumulation under laser pulse.

The NPC mechanism can be explained by considering the dominance of the photogating effect caused by the electron-hole pair photogeneration in Si or PtSe₂ close to the SiO₂ interface⁵⁶. When the device is irradiated, the incident laser is mostly absorbed by the Si substrate⁵⁷ leading to the creation of electron-hole pairs in the substrate. While the generated electrons are swept to ground, the photo-generated holes accumulate at the Si/SiO₂ interface or in SiO₂ trap states (see Figure 3(c)), favored by the vertical up-bending of the Si

bands at the Si/SiO₂ interface due to the different electron affinity of Si (~ 4.05 eV) and PtSe₂ (~ 4.6 eV), Figure 3(d).

The so-accumulated positive charge below the PtSe₂ channel plays the role of a positive gate voltage (photogating effect) which biases the device and decreases the channel current, according to the p-type behavior of the transistor.

The restoration of the initial state, in vacuum, is slower due to the limited diffusion of the positive photo-charge accumulated at the at the Si/SiO₂ interface or in the SiO₂ layer. It becomes faster in air because of the counterdoping effect of adsorbates, such as oxygen or water, which increase the p-doping of the PtSe₂ channel.

In conclusion, we investigated the electrical transport in PtSe₂ films along perpendicular directions. We used PtSe₂ as the channel material of field effect transistors in back-gated configuration. The conductance vs temperature behavior confirmed the semiconducting nature of ultrathin PtSe₂ films and the transistor characterization indicated intrinsic p-type conduction. The silicon back-gate enabled channel current modulation with field effect mobility up to ~ 40 cm²V⁻¹s⁻¹ at room temperature. The comparison of the channel conductance along perpendicular directions for a large number of devices led to the conclusion that the conduction is isotropic being mainly dominated by the polycrystalline structure of the PtSe₂ film. Finally, we found a negative photoconductivity under laser irradiation, indicating a dominant photogating effect.

Acknowledgments: This work is partially supported by Science Foundation Ireland (SFI) through grants 15/IA/3131 and 12/RC/2278 and 15/SIRG/3329, 12/RC/2278_P2 and by Italian Ministry of University and Research (MIUR), projects Pico & Pro ARS01_01061 and RINASCIMENTO ARS01_01088.

Data availability statement: The data that support the findings of this study are available from the corresponding author upon reasonable request.

References

- ¹ J. Huang, L. Yang, D. Liu, J. Chen, Q. Fu, Y. Xiong, F. Lin, and B. Xiang, *Nanoscale* **7**, 4193 (2015).
- ² Z. Lin, A. McCreary, N. Briggs, S. Subramanian, K. Zhang, Y. Sun, X. Li, N.J. Borys, H. Yuan, S.K. Fullerton-Shirey, A. Chernikov, H. Zhao, S. McDonnell, A.M. Lindenberg, K. Xiao, B.J. LeRoy, M. Drndić, J.C.M. Hwang, J. Park, Manish Chhowalla, R.E. Schaak, A. Javey, M.C. Hersam, J. Robinson, and M. Terrones, *2D Materials* **3**, 042001 (2016).
- ³ F. Urban, M. Passacantando, F. Giubileo, L. Lemmo, and A. Di Bartolomeo, *Nanomaterials* **8**, 151 (2018).
- ⁴ A. Di Bartolomeo, L. Genovese, F. Giubileo, L. Lemmo, G. Luongo, Tobias Foller, and M. Schleberger, *2D Materials* **5**, 015014 (2018).
- ⁵ L. Lemmo, F. Urban, F. Giubileo, M. Passacantando, and A. Di Bartolomeo, *Nanomaterials* **10**, 106 (2020).
- ⁶ F. Urban, N. Martucciello, L. Peters, N. McEvoy, and A. Di Bartolomeo, *Nanomaterials* **8**, 901 (2018).
- ⁷ A. Di Bartolomeo, F. Urban, M. Passacantando, N. McEvoy, L. Peters, L. Lemmo, G. Luongo, F. Romeo, and F. Giubileo, *Nanoscale* **11**, 1538 (2019).
- ⁸ A. Jawaid, D. Nepal, K. Park, M. Jespersen, A. Qualley, P. Mirau, L.F. Drummy, and R.A. Vaia, *Chem. Mater.* **28**, 337 (2016).
- ⁹ H. Li, G. Lu, Y. Wang, Z. Yin, C. Cong, Q. He, L. Wang, F. Ding, T. Yu, and H. Zhang, *Small* **9**, 1974 (2013).
- ¹⁰ M.-W. Lin, I.I. Kravchenko, J. Fowlkes, X. Li, A.A. Puretzky, C.M. Rouleau, D.B. Geohegan, and K. Xiao, *Nanotechnology* **27**, 165203 (2016).

- ¹¹ D. Lembke, A. Allain, and A. Kis, *Nanoscale* **7**, 6255 (2015).
- ¹² P. Johari and V.B. Shenoy, *ACS Nano* **6**, 5449 (2012).
- ¹³ Y. Jing, B. Liu, X. Zhu, F. Ouyang, J. Sun, and Y. Zhou, *Nanophotonics* **0**, (2020).
- ¹⁴ A. Di Bartolomeo, L. Genovese, T. Foller, F. Giubileo, G. Luongo, Luca Croin, S.-J. Liang, L.K. Ang, and M. Schleberger, *Nanotechnology* **28**, 214002 (2017).
- ¹⁵ A. Rai, J. H. Park, C. Zhang, I. Kwak, S. Wolf, S. Vishwanath, X. Lin, J. Furdyna, H. G. Xing, K. Cho, A. C. Kummel, and S. K. Banerjee, in *2018 76th Device Research Conference (DRC)* (2018), pp. 1–2.
- ¹⁶ F. Urban, F. Giubileo, A. Grillo, L. Lemmo, G. Luongo, M. Passacantando, T. Foller, L. Madau, E. Pollmann, M. Geller, D. Oing, M. Schleberger, and A. Di Bartolomeo, *2D Mater.* (2019).
- ¹⁷ B. Liu, M. Fathi, L. Chen, A. Abbas, Y. Ma, and C. Zhou, *ACS Nano* **9**, 6119 (2015).
- ¹⁸ C. Wang, K. Vinodgopal, and G.-P. Dai, in *Chemical Vapor Deposition for Nanotechnology*, edited by P. Mandracci (IntechOpen, 2019).
- ¹⁹ N. Huo, Y. Yang, Y.-N. Wu, X.-G. Zhang, S.T. Pantelides, and G. Konstantatos, *Nanoscale* **10**, 15071 (2018).
- ²⁰ G.Y. Guo and W.Y. Liang, *J. Phys. C: Solid State Phys.* **19**, 995 (1986).
- ²¹ C. Yim, V. Passi, M.C. Lemme, G.S. Duesberg, C. Ó Coileáin, E. Pallecchi, D. Fadil, and N. McEvoy, *Npj 2D Mater Appl* **2**, 5 (2018).
- ²² L. Li, K. Xiong, R.J. Marstell, A. Madjar, N.C. Strandwitz, J.C.M. Hwang, N. McEvoy, J.B. McManus, G.S. Duesberg, A. Goritz, M. Wietstruck, and M. Kaynak, *IEEE Trans. Electron Devices* **65**, 4102 (2018).
- ²³ P. Miró, M. Ghorbani-Asl, and T. Heine, *Angew. Chem. Int. Ed.* **53**, 3015 (2014).
- ²⁴ A. Di Bartolomeo, A. Pelella, X. Liu, F. Miao, M. Passacantando, F. Giubileo, A. Grillo, L. Lemmo, F. Urban, and S.-J. Liang, *Advanced Functional Materials* **29**, 1902483 (2019).
- ²⁵ A. Di Bartolomeo, F. Urban, A. Pelella, A. Grillo, M. Passacantando, X. Liu, and F. Giubileo, *Nanotechnology* (2020).
- ²⁶ A. Di Bartolomeo, A. Pelella, F. Urban, A. Grillo, L. Lemmo, M. Passacantando, X. Liu, and F. Giubileo, *Adv. Electron. Mater.* 2000094 (2020).
- ²⁷ H.L. Zhuang and R.G. Hennig, *J. Phys. Chem. C* **117**, 20440 (2013).
- ²⁸ Y. Wang, L. Li, W. Yao, S. Song, J.T. Sun, J. Pan, X. Ren, C. Li, E. Okunishi, Y.-Q. Wang, E. Wang, Y. Shao, Y.Y. Zhang, H. Yang, E.F. Schwier, H. Iwasawa, K. Shimada, M. Taniguchi, Z. Cheng, S. Zhou, S. Du, S.J. Pennycook, S.T. Pantelides, and H.-J. Gao, *Nano Lett.* **15**, 4013 (2015).
- ²⁹ L. Ansari, S. Monaghan, N. McEvoy, C.Ó. Coileáin, C.P. Cullen, J. Lin, R. Siris, T. Stimpel-Lindner, K.F. Burke, G. Mirabelli, R. Duffy, E. Caruso, R.E. Nagle, G.S. Duesberg, P.K. Hurley, and F. Gity, *Npj 2D Mater Appl* **3**, 33 (2019).
- ³⁰ L. Fang, W. Liang, Q. Feng, and S.-N. Luo, *J. Phys.: Condens. Matter* **31**, 455001 (2019).
- ³¹ C. Yim, N. McEvoy, S. Riazimehr, D.S. Schneider, F. Gity, S. Monaghan, P.K. Hurley, M.C. Lemme, and G.S. Duesberg, *Nano Lett.* **18**, 1794 (2018).
- ³² Z. Huang, W. Zhang, and W. Zhang, *Materials* **9**, 716 (2016).
- ³³ Y. Zhao, J. Qiao, Z. Yu, P. Yu, K. Xu, S.P. Lau, W. Zhou, Z. Liu, X. Wang, W. Ji, and Y. Chai, *Adv. Mater.* **29**, 1604230 (2017).
- ³⁴ W. Jiang, X. Wang, Y. Chen, G. Wu, K. Ba, N. Xuan, Y. Sun, P. Gong, J. Bao, H. Shen, T. Lin, X. Meng, J. Wang, and Z. Sun, *InfoMat* inf2.12013 (2019).
- ³⁵ J. Qiao, X. Kong, Z.-X. Hu, F. Yang, and W. Ji, *Nat Commun* **5**, 4475 (2014).
- ³⁶ Y. Zhao, J. Qiao, P. Yu, Z. Hu, Z. Lin, S.P. Lau, Z. Liu, W. Ji, and Y. Chai, *Adv. Mater.* **28**, 2399 (2016).
- ³⁷ W. Zhang, Z. Huang, W. Zhang, and Y. Li, *Nano Res.* **7**, 1731 (2014).
- ³⁸ X. Chia, A. Adriano, P. Lazar, Z. Sofer, J. Luxa, and M. Pumera, *Adv. Funct. Mater.* **26**, 4306 (2016).
- ³⁹ D. Hu, T. Zhao, X. Ping, H. Zheng, L. Xing, X. Liu, J. Zheng, L. Sun, L. Gu, C. Tao, D. Wang, and L. Jiao, *Angew. Chem. Int. Ed.* **58**, 6977 (2019).
- ⁴⁰ C. Yim, K. Lee, N. McEvoy, M. O'Brien, S. Riazimehr, N.C. Berner, C.P. Cullen, J. Kotakoski, J.C. Meyer, M.C. Lemme, and G.S. Duesberg, *ACS Nano* **10**, 9550 (2016).
- ⁴¹ T.-Y. Su, Y.-Z. Chen, Y.-C. Wang, S.-Y. Tang, Y.-C. Shih, F. Cheng, Z.M. Wang, H.-N. Lin, and Y.-L. Chueh, *J. Mater. Chem. C* **8**, 4851 (2020).
- ⁴² A. Kandemir, B. Akbali, Z. Kahraman, S.V. Badalov, M. Ozcan, F. Iyikanat, and H. Sahin, *Semicond. Sci. Technol.* **33**, 085002 (2018).

- ⁴³ M. O'Brien, N. McEvoy, C. Motta, J.-Y. Zheng, N.C. Berner, J. Kotakoski, K. Elibol, T.J. Pennycook, J.C. Meyer, C. Yim, M. Abid, T. Hallam, J.F. Donegan, S. Sanvito, and G.S. Duesberg, *2D Mater.* **3**, 021004 (2016).
- ⁴⁴ H. Zheng, Y. Choi, F. Baniasadi, D. Hu, L. Jiao, K. Park, and C. Tao, *2D Mater.* **6**, 041005 (2019).
- ⁴⁵ F. Urban, G. Lupina, A. Grillo, N. Martucciello, and A. Di Bartolomeo, *Nano Express* **1**, 010001 (2020).
- ⁴⁶ A. Grillo, A. Di Bartolomeo, F. Urban, M. Passacantando, J.M. Caridad, J. Sun, and L. Camilli, *ACS Appl. Mater. Interfaces* **12**, 12998 (2020).
- ⁴⁷ A. Pelella, O. Kharsah, A. Grillo, F. Urban, M. Passacantando, F. Giubileo, L. Iemmo, S. Sleziona, E. Pollmann, L. Madau, M. Schleberger, and A. Di Bartolomeo, *ArXiv:2004.00903 [Cond-Mat, Physics:Physics]* (2020).
- ⁴⁸ A. Ciarrocchi, A. Avsar, D. Ovchinnikov, and A. Kis, *Nat Commun* **9**, 919 (2018).
- ⁴⁹ C.S. Boland, C.Ó. Coileáin, S. Wagner, J.B. McManus, C.P. Cullen, M.C. Lemme, G.S. Duesberg, and N. McEvoy, *2D Mater.* **6**, 045029 (2019).
- ⁵⁰ F. Giubileo, A. Grillo, L. Iemmo, G. Luongo, F. Urban, M. Passacantando, and A. Di Bartolomeo, *Materials Today: Proceedings* **20**, 50 (2020).
- ⁵¹ A.D. Bartolomeo, F. Giubileo, F. Romeo, P. Sabatino, G. Carapella, L. Iemmo, T. Schroeder, and G. Lupina, *Nanotechnology* **26**, 475202 (2015).
- ⁵² E.A. Davis, *Solid-State Electronics* **9**, 605 (1966).
- ⁵³ Y. Han, X. Zheng, M. Fu, D. Pan, X. Li, Y. Guo, J. Zhao, and Q. Chen, *Phys. Chem. Chem. Phys.* **18**, 818 (2016).
- ⁵⁴ A. Serpi, *Phys. Stat. Sol. (a)* **133**, K73 (1992).
- ⁵⁵ G.Z. Liu, R. Zhao, J. Qiu, Y.C. Jiang, and J. Gao, *J. Phys. D: Appl. Phys.* **52**, 095302 (2019).
- ⁵⁶ F. Cadiz, C. Robert, G. Wang, W. Kong, X. Fan, M. Blei, D. Lagarde, M. Gay, M. Manca, T. Taniguchi, K. Watanabe, T. Amand, X. Marie, P. Renucci, S. Tongay, and B. Urbaszek, *2D Mater.* **3**, 045008 (2016).
- ⁵⁷ A. Francinelli, D. Tonneau, N. Clément, H. Abed, F. Jandard, S. Nitsche, H. Dallaporta, V. Safarov, and J. Gautier, *Appl. Phys. Lett.* **85**, 5272 (2004).